Power Distribution Control and Performance Assessment of a Wind Energy fed Microgrid Integrated with Hybrid Energy Storage System

Pradyumna Kumar Behera, *Student Member, IEEE,* Monalisa Pattnaik, *Senior Member, IEEE*
Department of Electrical Engineering, National Institute of Technology Rourkela, 769008, Odisha, India

Abstract

The present work proposes a coordinated power distribution control of wind-energy fed self-excited induction generator (SEIG) based low-voltage direct current (LVDC) autonomous microgrid. The battery and supercapacitor (SC) hybrid energy storage system (HESS) is interfaced with the common 48 V LVDC bus using a parallel-active configuration through two bidirectional converters. The prime idea of hybridization is to limit the instantaneous peak current demand and also to alleviate the charge/discharge stress during transients, thus reducing the size of the battery. The developed autonomous LVDC system with the supervisory power distribution control scheme (PDCS) is experimentally validated for different operating modes. The comparative experimental result analysis substantiates the efficacy of the proposed PDCS along with seamless transition between various modes.

Index Terms

Charge/discharge control, Hybrid energy storage system, Microgrid, Power distribution control scheme, Wind power generation system

I. Introduction

THE prime consensus of Energy Strategy (ES2050) urge the augmentation of renewable energy (RE) usage combined with intensified electrification to meet the escalated power demand and establishment of a sustainable future [1]. Further, after the Covid-19 pandemic, the global recuperation process made it mandatory to develop greener electrification systems, leading to substantial rise in RE sector. In this context, renewable energy sources (RESs) such as wind and PV can play a crucial role in bringing the synergy between power generation and the end-use demand in the global energy-mix and also help in cruising down the CO_2 emissions [2]. For enabling the transition from traditional power system to future smart grid, renewable energy powered microgrid concept have been developed. In general terms, smart microgrids (SMG) are intelligent and an aggregated system consisting of several heterogeneous distributed energy resources (DERs), storage systems, dispersed loads (DLs) and power electronic converters. They are particularly deployed at the site of use and can seamlessly connect and disconnect with utility grid [3], [4]. The power output from wind power generation being recurrent/intermittent calls for inclusion of energy storage systems (ESSs) to fulfill the continuous load requirement [5], [6]. Amongst various energy storage options, battery is widely used for addressing following tasks: (a) store the excess generated power; (b) assist in fulfillment of load demand when generation is limited; (c) DC bus voltage regulation [7]. However, battery-based energy storage system (ESS) suffers certain challenges such as low power density and fast battery health degradation due to high and frequent charge/discharge rate in applications requiring instantaneous power [8], [9]. The negative impact due to aforementioned drawbacks are characterised by battery state of health (SOH), can be seen from battery degradation analysis [10], [11]. Further, higher c-rating and depth of discharge (DOD) expedite the capacity fading in batteries [12]. For systems requiring frequent and high-rate charging/discharging, extra ESS or a buffer is essential to deal the surge current. Supercapacitor (SC) exhibits high power density, yet lower energy density in contrast to battery allowing them well suited for short-term transients [13], [14]. The DC-bus voltage, battery, and SC current responses for step change in load and generation are delineated in Fig.1 (a) and (b) respectively. The hybridization of energy storage using a combination of battery and SC has potential to circumvent the demerits of battery usage as sole energy storage and improve the system overall efficiency [13]–[15]. With this motivation, the possible architectures for assimilation of battery and SC in a microgrid or electric vehicle applications forming the hybrid energy storage system (HESS) are evolved [16], [17]. Similarly, the development of power electronic converters, their interconnection topologies, and the formulation of various control strategies are major research areas in a DC microgrid (DCMG). Depending on the topology, power distribution approach can be developed to manage the power flow while ensuring proper performance within the operational boundaries of DCMG. The operation of HESS in a LVDC microgrid demands for a coordinated control and comprehensive power distribution control scheme (PDCS) to regulate the power flow reaping the individual merits of SC and battery. Broadly, the DCMG power management control approach is classified into two major categories [16]–[19] i.e. (a) rule-based techniques (RBTs) and (b) optimization based strategies (OBSs). Various RBTs are based on filtration [20], fuzzy logic [21], dead-beat [22], sliding mode [23] and droop control [24]. The filtration based RBT involves an easy real-time implementation with simple rules to decouple the high and low frequency components of the SC and battery current. But, certain trade-off with parameter constraints (like time constant of low pass filter (LPF), control bandwidth etc.) should be taken

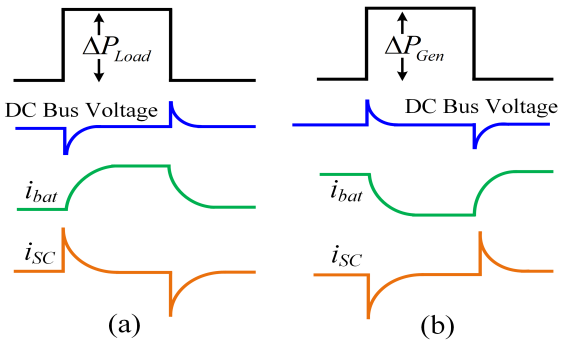

Fig. 1: DC-bus voltage and battery, supercapacitor current response for (a) step change in load demand (b) step change in generation

into account. Likewise, OBSs are categorized into two methods i.e. namely online and offline methods [25]. Unlike RBTs, OBSs require large data storage, rigorous data training and complex mathematical computations.

Due to simplicity and easy implementation, filtration based RBTs with power management for a photovoltaic (PV) fed DCMG is well explored in literature. Further, the integration of HESS either in a standalone or a grid-connected PV system are also widely investigated in various research articles [14], [26]–[31]. However, the HESS integration with wind system is little explored. As the power fluctuation associated with WPGS compared to a PV system is more due to rapid variations in wind speed, the deployment of battery-SC based HESS is very essential. To mitigate these power oscillations and to reduce the size of the battery, incorporation of SC along with battery is a promising solution in a wind energy fed DCMG for smoothing the short-term as well as long-term power variations. In this article, an effort has been made to improve the overall performance of the wind-driven LVDC microgrid with an integrated HESS. The system is capable of achieving proper power sharing at different operating modes. The key contributions of this article are delineated below.

1) A parallel active HESS topology is integrated with a small-scale WPGS based LVDC microgrid. For proper design and development of the LVDC microgrid, the bidirectional converters are designed and small-signal stability analysis is done.
2) In the HESS controller, the outer voltage loop generates the net reference current to maintain the DC bus voltage at 48 V. For generation of battery and SC reference current, the net current is splitted into average and dynamic part.
3) Further, in the proposed controller, the battery uncompensated current is diverted to the SC for quicker restoration of DC bus voltage during dynamic instants. Thus, improving the overall system response.
4) The coordinated power sharing among the SEIG based WPGS and HESS with its charge/discharge control in the developed LVDC microgrid is achieved during different operating modes. The PDCS regulates the DC bus voltage tightly during sudden load and wind speed variations.
5) The proposed and conventional controller performance is verified in the developed HESS integrated LVDC test-rig. The comparative result analysis is showcased for wind speed and load variation under normal operating modes ($50\% < SOC < 90\%$).
6) Also, the PDCS is effective in handling battery protection mode as well as reduced power mode during load shedding. The seamless mode transition and improved dynamic response confirms the effectiveness of the proposed PDCS.

II. LVDC Microgrid Architecture

A DCMG comprising the wind power generation system (WPGS), hybrid energy storage system (HESS) and DC load is delineated in Fig. 2. The wind system is connected to the DC bus through a buck converter and by varying the duty ratio (D_{bu}), the operating point of the WPGS can be aligned at the optimum point to extract the peak power. The HESS combines the advantages of both battery and SC to overcome the intermittency associated with WPGS. Here, the both the storage units are linked through a parallel active configuration of two bidirectional DC-DC converters. The autonomous DC microgrid mostly leverage on HESS to regulate the DC bus voltage and also maintain the power balance during supply-demand disparity. The aim of the design and implementation of the DCMG focuses primarily on stabilization of the DC bus voltage and development of supervisory power distribution technique to coordinate DERs, storage and loads.The appropriate filter parameters of the buck converter and bidirectional converters (BDC) are designed as shown below:

A. Design of Buck Converter Parameters for WPGS

By varying the duty ratio (D_w) of the buck converter, the operating point of the WPGS can be aligned at the optimum point to extract the peak power. The design of the appropriate filter parameters are designed as per [32], [33]. The value of inductor (L_w) is as follows:

$$L_w = \frac{V_{dc}(1 - D_{bu})}{\Delta I_w \times f_s} \tag{1}$$

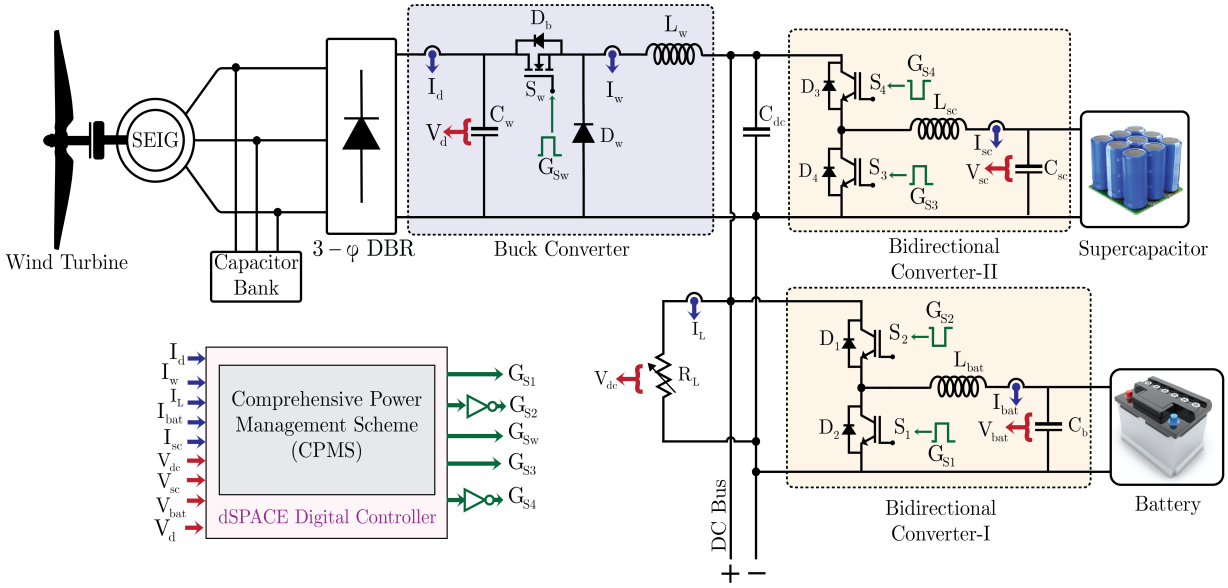

Fig. 2: Circuit diagram of wind energy driven LVDC microgrid

where, $V_{dc} = D_{bu}.V_d$. The parameters V_d, V_{dc}, f_s and D_{bu} depicts the input voltage, load voltage, switching frequency and duty ratio of the buck converter respectively.

B. Design of Bidirectional Converter Parameters for HESS

The filter parameters of the bidirectional DC-DC converter are designed according to [32], [33]. Both the converters are assumed to be operating in CCM mode. The minimum filter inductance (L_{bat}) and capacitance (C_{dc}) for the bidirectional converter-I (BDC-I) can be calculated as [34]:

$$L_{bat} = \frac{V_{bat}(1 - \frac{V_{bat}}{V_{dc}})}{f_{sw} \times \Delta I_{bat}} \tag{2}$$

$$C_{dc} = \frac{V_{dc} D_{bat}}{R_L \times \Delta V_{dc} \times f_{sw}} \tag{3}$$

where, V_{bat}, V_{dc}, f_{sw} R_L and D_{bat} represents the battery voltage, DC-bus voltage, switching frequency, load resistance and duty cycle of the converter respectively. In the similar way, the filter parameter (L_{sc}) for the bidirectional converter-II (BDC-II) can also be calculated. While designing these converters, inductor current ripple (ΔI) and DC-bus voltage ripple (ΔV_{dc}) for the converters are limited to 10% and 1% respectively. The filter parameters are provided in Table. I. The control of the designed buck converter and bidirectional converters by the comprehensive power management scheme (CPMS) is depicted in the next section.

III. Controller Design for LVDC Microgrid

A. Controller Design of WPGS

1) MPPT Controller: To increase the efficiency of the hybrid system, performance of the MPPT controller plays a vital role. Hence, to harness the optimum power from the WPGS irrespective of climatic conditions, a modified drift-free perturb and observe (DF-P&O) maximum power point tracking (MPPT) technique is incorporated [35]. The DF-P&O MPPT avoids drift under sudden wind speed change conditions.

2) Reduced Power Mode (RPM) Controller: Whenever wind power generation is excess than load demand and the SOC of the battery is $\geq$ 90%, reduced power mode is activated and simultaneously, the battery controller is disconnected. This controller is proposed for the protection of battery from getting overcharged and the operating point of WPGS is shifted from MPP to a reduced power point. Similarly, for SOC $\leq$ 50% and wind power lesser than load demand, reduced power mode along with load shedding is implemented to protect battery from deep discharging. Here, a cascaded two loop control of the buck converter is implemented to maintain DC bus voltage constant.

B. Design of proposed controller for HESS

The proposed power management scheme mainly generates the reference current and maintains the DC-bus voltage. Initially, the PDCS utilizes the existing control technique [36] for power distribution among the DERs, load and HESS. Then the proposed HESS controller is thoroughly analyzed and designed, the steps are articulated below.

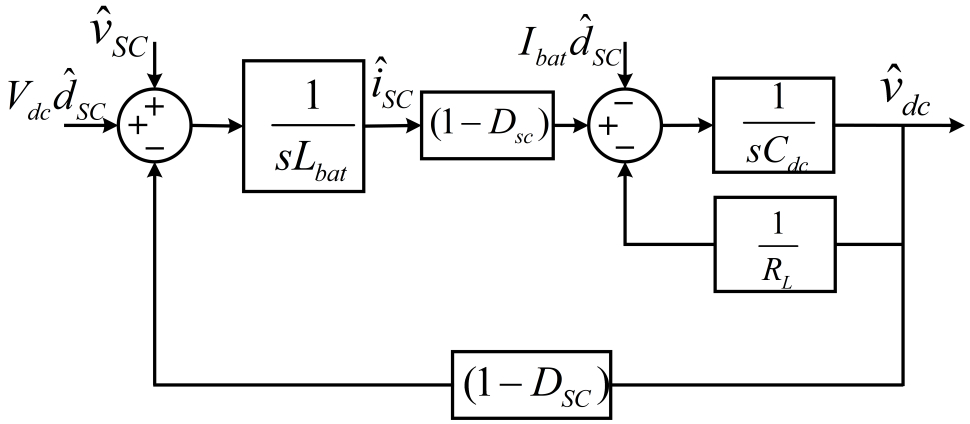

Fig. 3: Small-signal model of bidirectional converter

1) Generation of reference current: The power balance among the DER, HESS and load present in the LVDC microgrid are attained by maintaining a constant DC-bus voltage irrespective of different operating conditions. The DC-bus voltage regulator generates the net reference current ($i_{net}(t)$) to be drawn/supplied from/into the DC-bus in order to maintain the reference bus voltage.

$$v_e(t) = v_{dc\_ref}(t) - v_{dc} \tag{4}$$

$$i_{net}(t) = k_{p\_vdc}v_e(t) + k_{i\_vdc}\int v_e(t) \tag{5}$$

where, k_{p_vdc} and k_{i_vdc} are the PI controller gains. It can be inferred that $i_{net}(t) < 0$ whenever v_e is negative, which implies

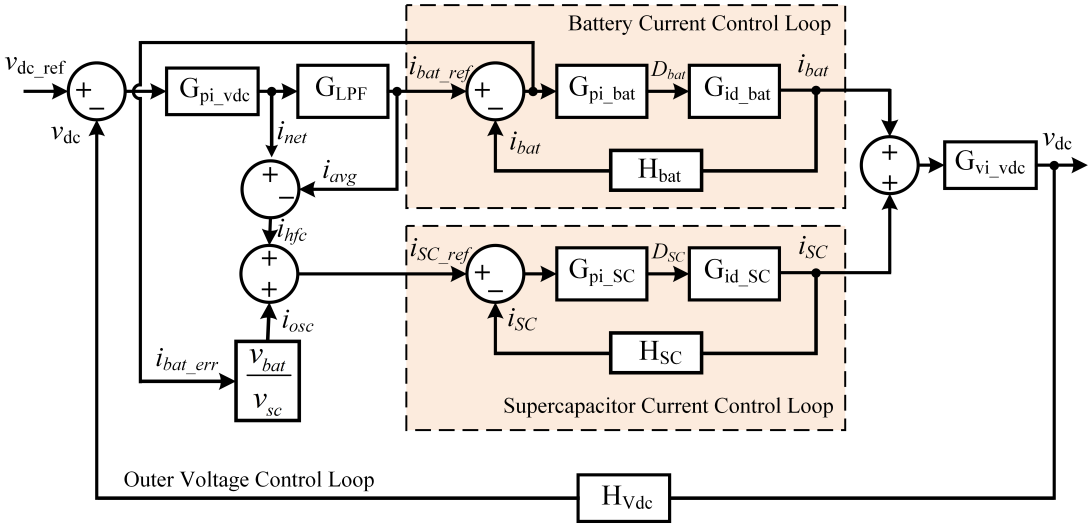

Fig. 4: Small-signal model of HESS controller

that the DC-bus power is less than the load power and vice-versa. This characteristic of i_{net} is used to determine different operating mode of the LVDC microgrid. The power in the microgrid under various supply and load conditions should be balanced as follows:

$$P_{net}(t) = P_w(t) - P_{load}(t) - P_{loss}(t) \tag{6}$$

where, $P_{net}(t) = P_{bat}(t) + P_{SC}(t)$ is the total power required to regulate the DC-bus voltage, P_w is the wind power, P_{load} is the load power, and P_{loss} is the total power loss in the DC microgrid. This net power is absorbed/supplied by the HESS depending upon generation and demand disparity.

The net reference current is passed through a low-pass filter to extract the average current component as delineated in Eq. (5). The LPF cut-off frequency is selected to be 5 Hz. The rate-limiter restricts the charge/discharge rates of the battery bank within the safe limits.

$$i_{avg}(t) = i_{bat\_ref} = i_{net}(t).\frac{\omega_c}{\omega_c + s} \tag{7}$$

$$i_{tra}(t) = \underbrace{(1 - \frac{\omega_c}{\omega_c + s})i_{net}(t)}_{i_{hfc}} + \underbrace{\left(\frac{v_{bat}}{v_{sc}}\right) i_{bat\_err}}_{i_{osc}} \tag{8}$$

The former part in Eq. (8) represents the high-frequency component ($i_{hfc}(t)$) and the latter part depicts the oscillatory component ($i_{osc}(t)$) in which uncompensated battery current or battery error current is taken into account. The PDCS allocates the transient component ($i_{tra}(t)$) to the SC which is given in Eq. (8). The diversion of uncompensated battery current to the SC improves the system response and helps in quicker restoration of the DC-bus voltage. The generated supercapacitor and battery reference currents are compared with the actual currents (Fig. 6). The error signals are fed through the PI controllers for generation of duty ratios (i.e. D_{bat} in case of BDC-I and D_{SC} for BDC-II), which are used to generate switching pulses for both the converters.

2) Small-signal and Stability Analysis of the LVDC microgrid: After the formulation of reference current, the foremost step towards design of controller is the small-signal analysis of the converter. For both the bidirectional converters (BDC) depicted in Fig. 2, the control switches S_1, S_2 and S_3, S_4 operates in complementary manner to each other. Thus, both the BDC share similar transfer function during boost as well as buck mode having same small-signal model which is shown in Fig. 3. For this analysis, the boost mode operation is taken into account to make it simple, clear and concise. As, the SC exhibits quicker dynamic response in comparison with the battery, the PI controller parameters are designed according to the SC stage. Therefore, the averaged state-space equations of only BDC-II is considered and derived as follows.

$$L_{SC}\frac{di_{SC}}{dt} = v_{SC}(t) - (1 - d_{SC}(t))v_{dc}(t) \tag{9}$$

$$C_{dc}\frac{dv_{dc}(t)}{dt} = (1 - d_{SC}(t))i_{SC}(t) - \frac{v_{dc}(t)}{R_L} \tag{10}$$

where, i_{SC}, v_{SC}, d_{SC} and v_{dc} represent SC current, SC voltage, duty ratio and DC-bus voltage. The design of feedback control technique primarily requires the linearized state-space equations around the equilibrium point with small-signal perturbations. The state parameters of the system are depicted below.

$$v_{dc}(t) = V_{dc} + \hat{v}_{dc}(t); i_{SC}(t) = I_{SC} + \hat{i}_{SC}(t); \tag{11}$$

$$v_{SC}(t) = V_{SC} + \hat{v}_{SC}(t); d_{SC}(t) = D_{SC} + \hat{d}_{SC}(t) \tag{12}$$

Neglecting the second-order small-signal entities, the averaged equations can be represented as:

$$L_{SC}\frac{d\hat{i}_{SC}(t)}{dt} \simeq \hat{v}_{SC}(t) - (1 - D_{SC})\hat{v}_{dc}(t) + V_{dc}\hat{d}_{SC}(t) \tag{13}$$

$$C_{dc}\frac{d\hat{v}_{dc}(t)}{dt} \simeq (1 - D_{SC})\hat{i}_{SC}(t) - I_{SC}\hat{d}_{SC}(t) - \frac{\hat{v}_{dc}(t)}{R_L} \tag{14}$$

Applying Laplace-transformation to above equations and simplifying, it can be written as:

$$\hat{i}_{SC}(s) \simeq \frac{\hat{v}_{SC}(s) - (1 - D_{SC})\hat{v}_{dc}(s) + V_{dc}\hat{d}_{SC}(s)}{sL_{SC}} \tag{15}$$

$$\hat{v}_{dc}(s) \simeq \frac{C_{dc}(1 - D_{SC})\hat{i}_{SC}(s) - I_{SC}\hat{d}_{SC}(s) - \frac{\hat{v}_{dc}(s)}{R_L}}{sC_{dc}} \tag{16}$$

The equations in (15) and (16) delineates the frequency domain model of the bidirectional converter during boost mode. Upon rearranging these equations, various transfer function of the converter can be obtained. The small-signal analysis of BDC-I with battery as input can be done similarly. To assure the complete system stability, the bandwidths (BW) for various control loops are selected and the gain values of different PI controller are tuned.

a) Supercapacitor Inner Current Control Loop Design: The transfer function of control ($\hat{d}_{SC}$) to SC current ($\hat{i}_{SC}$) is found as:

$$\begin{aligned} G_{id\_SC}(s) = \frac{\hat{i}_{SC}(s)}{\hat{d}_{SC}(s)} &= \frac{2(1 - D_{SC})I_{SC} + V_{dc}C_{dc}}{(1 - D_{SC})^2 + \frac{sL_{SC}}{R_L} + L_{SC}C_{dc}s^2} \\ &= \frac{0.1056s + 4}{2.2 \times 10^{-6}s^2 + 4.167 \times 10^{-5}s + 0.5625} \end{aligned} \tag{17}$$

Then, the open-loop transfer function of the SC current control loop can be determined using Eq. (18) and the corresponding Bode-plot is represented in Fig. 5(a).

$$G_{ol\_SC} = G_{pi\_SC}.G_{id\_SC}.H_{SC} \tag{18}$$

where, G_{pi_SC} represents the transfer function of the SC current loop compensator.

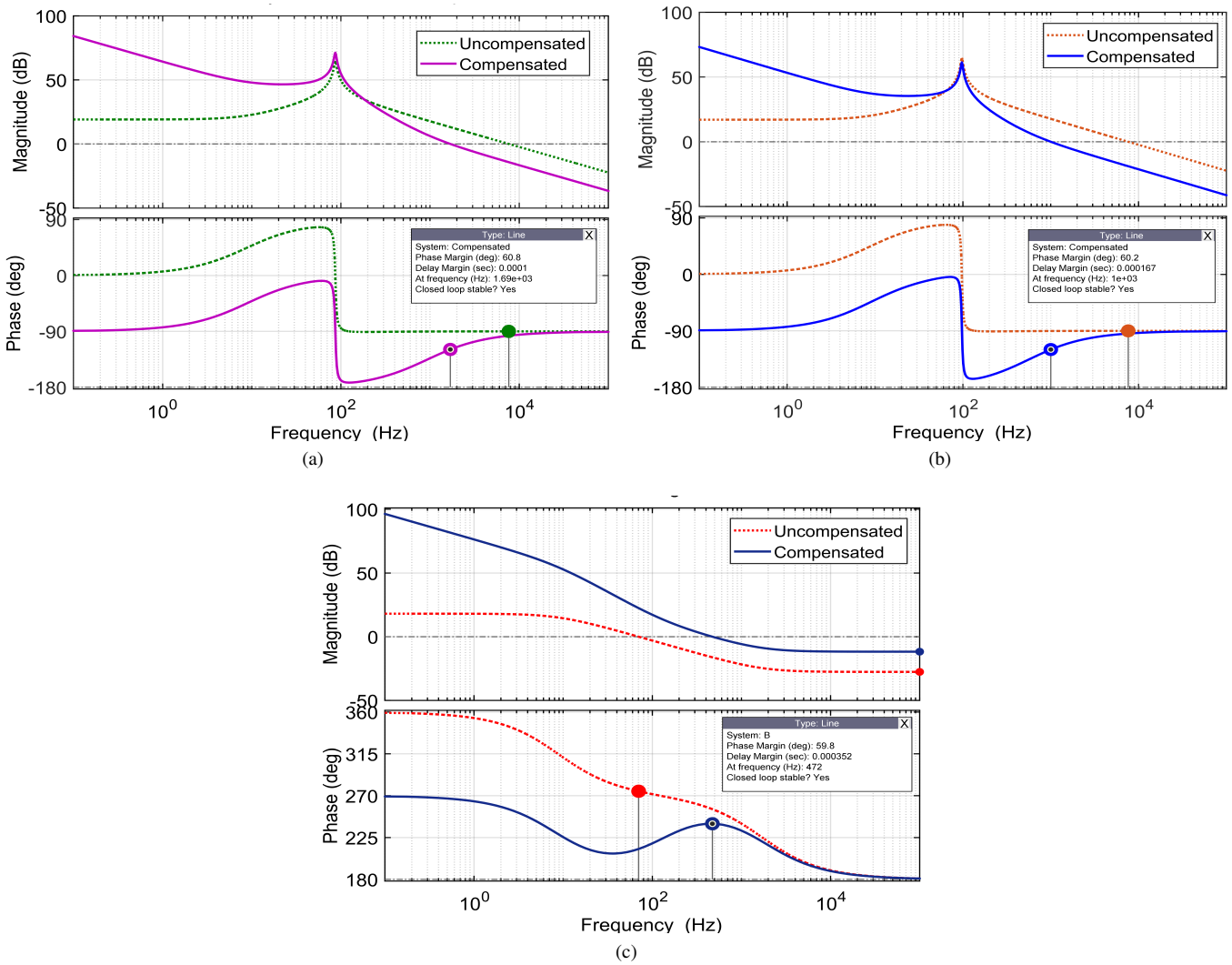

Fig. 5: Bode-plot of different control loops (a) SC current control (b) battery current control (c) Outer-loop voltage control

b) Battery Inner Current Control Loop Design: The transfer function of control ($\hat{d}_{bat}$) to battery current ($\hat{i}_{bat}$) is:

$$G_{id\_bat}(s) = \frac{\hat{i}_{bat}(s)}{\hat{d}_{bat}(s)} = \frac{2(1-D_{bat})I_{bat} + V_{dc}C_{dc}}{(1-D_{bat})^2 + \frac{sL_{bat}}{R_L} + L_{bat}C_{dc}s^2} = \frac{0.1056s + 4}{2.2 \times 10^{-6}s^2 + 4.167 \times 10^{-5}s + 0.4444} \tag{19}$$

Using Eq. (20), the open-loop transfer function of the battery current control loop can be determined and the corresponding Bode-plot is shown in Fig. 5(b).

$$G_{ol\_bat} = G_{pi\_bat}.G_{id\_bat}.H_{bat} \tag{20}$$

where, G_{pi_bat} represent the transfer function of battery current compensator.

$$\hat{i}_{SC}(s) \simeq \frac{\hat{v}_{SC}(s) - (1-D_{SC})\hat{v}_{dc}(s) + V_{dc}\hat{d}_{SC}(s)}{sL_{SC}} \tag{21}$$

$$\hat{v}_{dc}(s) \simeq \frac{C_{dc}(1-D_{SC})\hat{i}_{SC}(s) - I_{SC}\hat{d}_{SC}(s) - \frac{\hat{v}_{dc}(s)}{R_L}}{sC_{dc}} \tag{22}$$

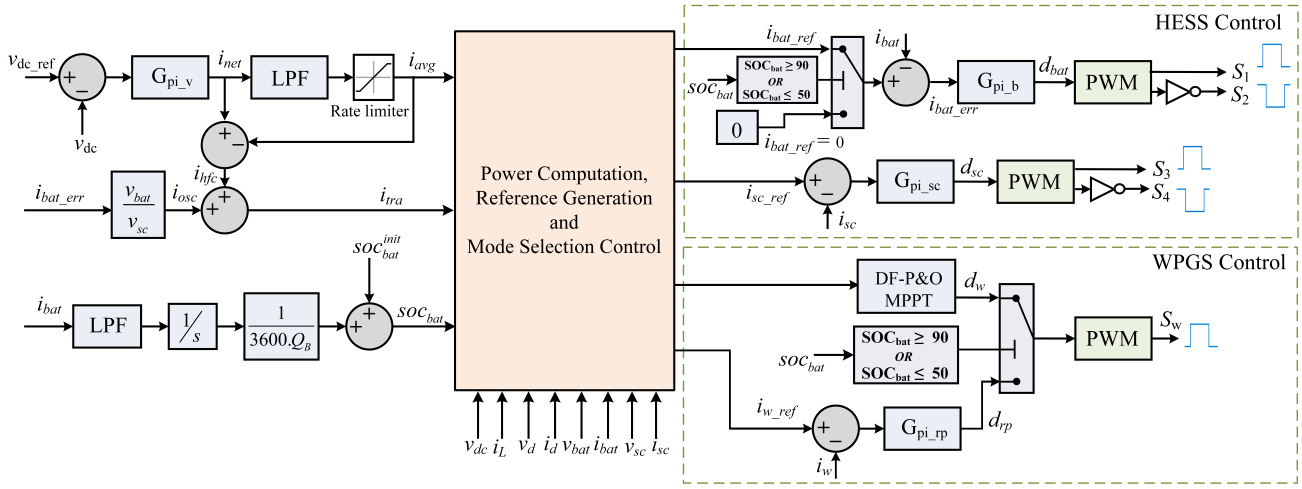

Fig. 6: Detailed block diagram of power distribution control scheme

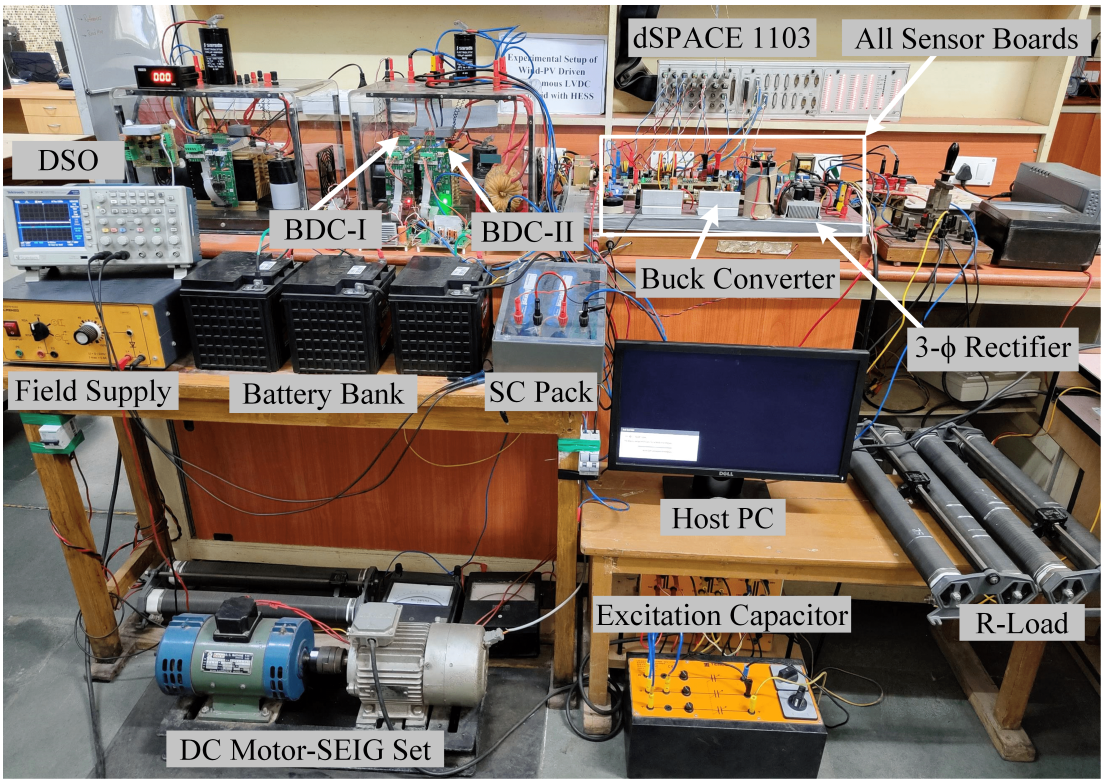

Fig. 7: Experimental test-rig of autonomous LVDC microgrid

c) Outer Voltage Control Loop Design: The transfer function of the supercapacitor current to the DC-bus voltage transfer function is given as:

$$G_{vi\_Vdc}(s) = \frac{\hat{v}_{dc}}{\hat{i}_{SC}} = \frac{V_{dc} - D_{SC}V_{dc} - L_{SC}I_{SC}s}{2I_{SC} - 2D_{SC}I_{SC} + C_{dc}V_{dc}s} = \frac{31.68 - 2.5 \times 10^{-3}s}{3.3 + 0.1056s} \tag{23}$$

The open loop transfer function can be depicted as:

$$G_{ol\_vdc} = G_{pi\_vdc}.G_{cl\_SC}.G_{vi\_vdc}.H_{Vdc} \tag{24}$$

where,

$$G_{cl\_SC} = \frac{G_{pi\_SC}.G_{id\_SC}}{H_{SC}.G_{pi\_SC}.G_{id\_SC} + 1} \tag{25}$$

TABLE I: Autonomous LVDC microgrid parameters

DC- bus voltage = 48 V, Load resistance (R_L) = 24 Ω, 12 Ω
DC motor-SEIG based WPGS
Rectifier Module: EK.IR.MDS100165 Buck Converter: Switch: IRFP460, Diode: MUR3060PT, Driver: TLP350 C_d = 1200 μF, L_w = 2.5 mH, f_{sw} = 10 kHz
HESS Parameters
Lead-acid battery (Exide-FE-04-EP42-12): 12V, 42 Ah, 3 no.s Supercapacitor (BMOD0058E016 B02): 16.2 V, 58 F, 2 no.s Bidirectional Converter (2 nos.):Switch:IGBT Leg (SKM100GB063D), IGBT Driver: Skyper32 C_{dc} = 2200 μF, L_{bat} = L_{sc} = 1 mH, f_{sw} = 10 kHz
Other Components
Voltage Transducer: LV-25P, Current Transducer: LEM-55P Digital Controller: dSPACE 1103, Sampling Time: 20 μs

TABLE II: PI controller parameters

Control Loop	Bandwidth (Hz)	PM	PI Values
SC Current Control Loop	1690 Hz	60.8°	k_{p_SC} = 0.1927 k_{i_SC} = 1133.8
Battery Current Control Loop	1000 Hz	60.2°	k_{p_bat} = 0.1131 k_{i_bat} = 404.2
Outer Voltage Control Loop	470 Hz	59.8°	k_{p_vdc} = 0.1054 k_{i_vdc} = 102.4

The Bode-plot of the outer voltage control loop is given in Fig. 5(c). The equivalent small signal model of the HESS controller is depicted in Fig.4. For all the three control loops, the phase margin is around 60° and the corresponding BW as well as exact PI values are depicted in Table II. In the next section, the power management strategy for deciding the various operating modes of the LVDC microgrid is discussed.

IV. Power Distribution Control Scheme

The PDCS is formulated to attain the following objectives:

1) Stabilization of DC-bus voltage to maintain optimal power balance among the source and load with proper charging/discharging rate of the HESS.
2) Segregation of total reference current and allocation of average and transient component to battery and SC respectively.
3) Identification of operating modes of the LVDC microgrid based on various constraints and assuring smooth transition from one operating mode to the appropriate mode.
4) Protection of battery to avoid deep-discharge and overcharge conditions by disconnecting the battery and simultaneously switching of WPGS from MPPT to RPM.

The PDCS mainly decides the operating mode of the LVDC microgrid based on the available power generation and load demand (Fig. 6). The power disparity is fulfilled by the HESS according to the state-of-charge (SOC). There are four working conditions or sub-modes that are decided by the power management algorithm: (a) excess generation mode (EGM) (i.e. $P_w > P_{load}$) (b) deficit generation mode (DGM) (i.e. $P_w < P_{load}$) (c) floating power mode (FPM) (i.e. $P_w \simeq P_{load}$) (d) RPM (i.e. $SOC \geq 90\%$ or $SOC \leq 50\%$)

A. Mode: I- Normal Operating Condition ($SOC_L < SOC < SOC_U$):

This mode deals with charging/discharging of the battery stack when the state of charge of the battery is in between SOC_L and SOC_U. In this paper, lower and upper threshold limit of SOC is considered 50% and 90% respectively. During this mode, WPGS harness optimum power and whenever the extracted wind power is excess than the load demand, the HESS absorbs the surplus power. In other words, the net available power $P_{net}(t)$ is absorbed by the battery along with the supercapacitor maintaining a constant DC-bus voltage. The system is considered to be operating under excess generation mode (EGM). Similarly, if wind power is less than load demand, the system operates under deficit generation mode (DGM). And, if the available wind power is equal to the load demand, then the system operates at floating power mode (FPM). During transient instants, the controller provides the average component to the battery and diverts the high frequency and oscillatory component

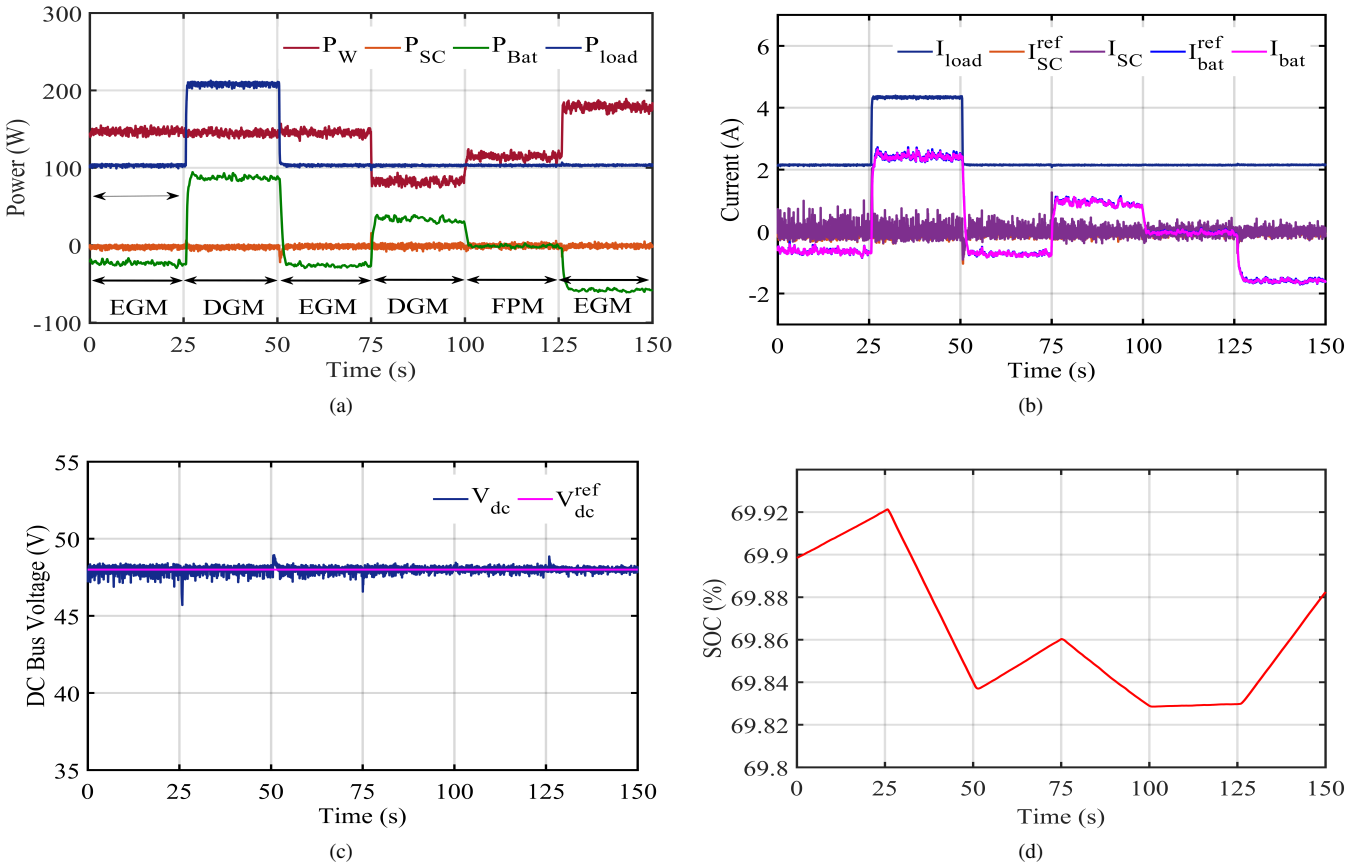

Fig. 8: Experimental results during mode-I operation with the proposed controller (a) power (b) battery, SC and load current (c) DC bus voltage, (d) % SOC of the battery

towards SC relieving the stress on the battery. The power balance equation is represented below:

$$P_{load}(t) = \begin{cases} \underbrace{P_w(t) - P_{net}(t) - P_{loss}(t) \ if \ P_w(t) > P_{load}(t)}_{EGM} \\ \underbrace{P_w(t) + P_{net}(t) - P_{loss}(t) \ if \ P_w(t) < P_{load}(t)}_{DGM} \\ \underbrace{P_w(t) - P_{loss}(t) \ if \ P_{net}(t) = 0}_{FPM} \\ \underbrace{P_{net}(t) \ if \ P_w(t) = 0}_{DGM} \end{cases} \tag{26}$$

B. Mode: II- Battery Protection Mode:

This mode deals with the protection of battery from overcharge and deep-discharge considering %SOC as the major constraint.

1) $SOC_{bat} \geq 90\%$: In this mode, if the SOC of the battery is more than 90% and the power generated by wind system is in excess to the load demand, the PDCS stops the battery controller operation. Simultaneously, the operating point of the WPGS shifts from MPP to reduced power mode. In the above scenario, the DC bus voltage can not be maintained at 48 V if reduced power mode is not activated from the instant PDCS executes battery shutdown.

$$P_{load}(t) = \underbrace{P_{wrp}(t) - P_{loss}(t), P_{net}(t) = 0}_{if \ P_{wmpp} > P_{load} \text{ and } SOC \geq SOC_U} \tag{27}$$

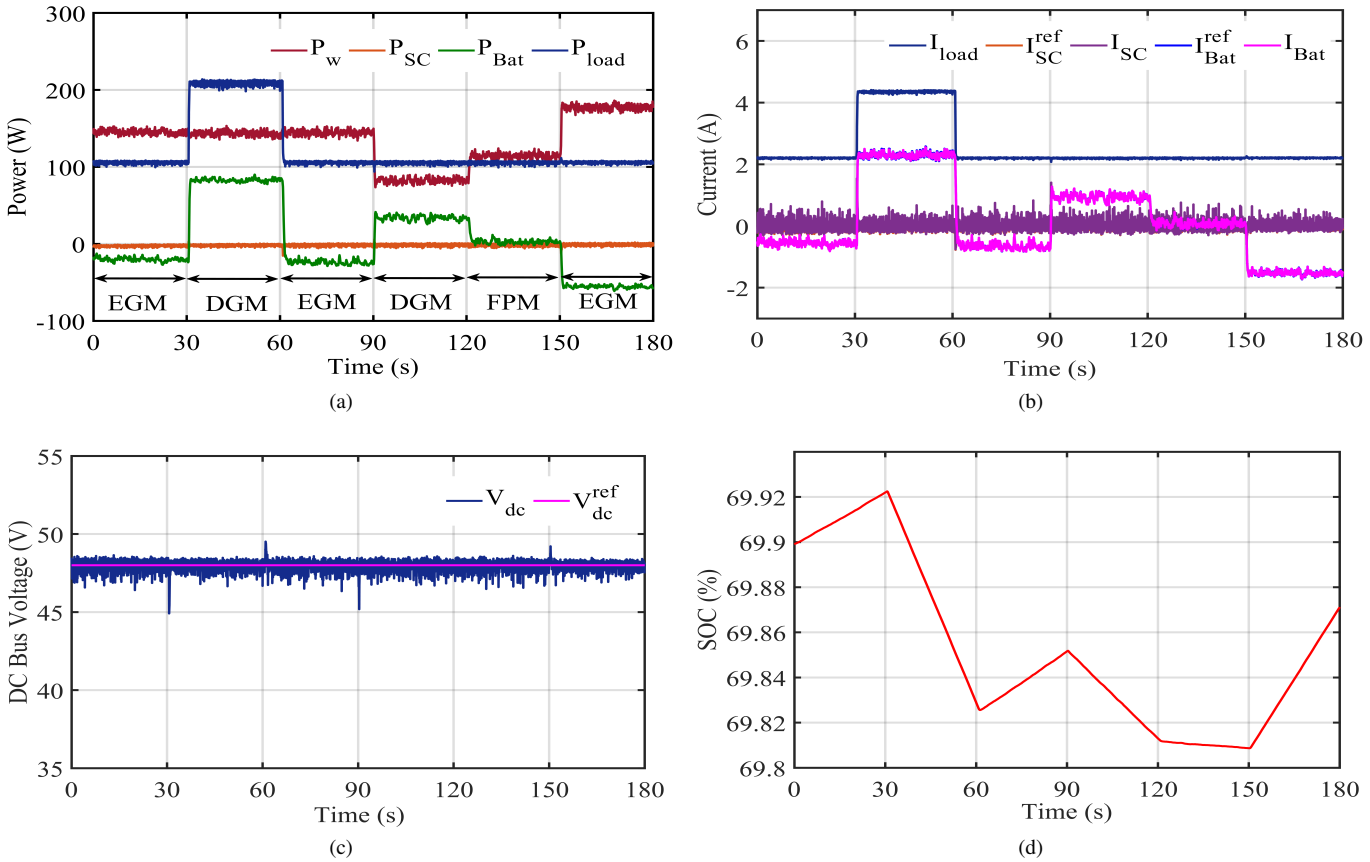

Fig. 9: Experimental results during mode-I operation with the conventional controller (a) power (b) battery, SC and load current (c) DC bus voltage, (d) % SOC of the battery

2) $SOC_{bat} \leq 50\%$*:* Whenever the power generation of WPGS is less than the load requirement and SOC of the battery is less than equal to SOC_L, to prevent battery from deep discharge, the PDCS stops the battery controller operation.

$$P_{load}(t) = \underbrace{P_{wrp}(t) - P_{loss}(t), P_{net}(t) = 0}_{if\ \ P_{wmpp} < P_{load} \text{ and } SOC \leq SOC_L} \tag{28}$$

Under this condition, as the load demand is more than the power generation of the WPGS, load shedding is incorporated.

C. Performance Validation of the LVDC Microgrid:

A laboratory test-rig of the wind energy driven LVDC microgrid with HESS is developed for the performance validation of the proposed power distribution control scheme using dSPACE DS1103 digital controller. The system and PDCS control parameters are depicted in Table I and Table II respectively. The photograph of the laboratory test-bed is shown in Fig. 6. The experimental results and analysis under different operating mode is illustrated briefly in next subsections. To show the functionality of the proposed PDCS more precisely, this section is divided into two case studies i.e. normal operating mode and battery protection mode.

1) Normal operating mode ($50\% < SOC < 90\%$*):* In this mode, the performance of the PDCS is shown for load and wind speed variation. The experimental results during this mode with proposed and conventional controller are shown in Fig. 8 and Fig. 9 respectively. The power balance along with reference current generation for different sub-modes with respective time interval are clearly depicted in Table III. In Fig. 10, comparative results of the conventional and proposed controller under sudden load and wind speed variation is depicted. It can be seen that the DC bus voltage is maintained at 48 V despite variations in load demand and wind speed.

2) Battery Protection Mode: : Whenever the %SOC of the battery crosses the safe limits (i.e. either $SOC \geq 90\%$ or $SOC \leq 50\%$), the PDCS disconnects the battery by making the battery reference current to zero. The experimental results of the proposed and existing controller for battery shutdown mode are given in Fig. 11 and Fig. 12 respectively. Similarly, the experimental results for $SOC \leq 50\%$ are shown in Fig. 13 and Fig. 14 respectively. The power balance and reference current under these modes are also provided in Table III. During all these operating conditions, it can be seen that the PDCS is

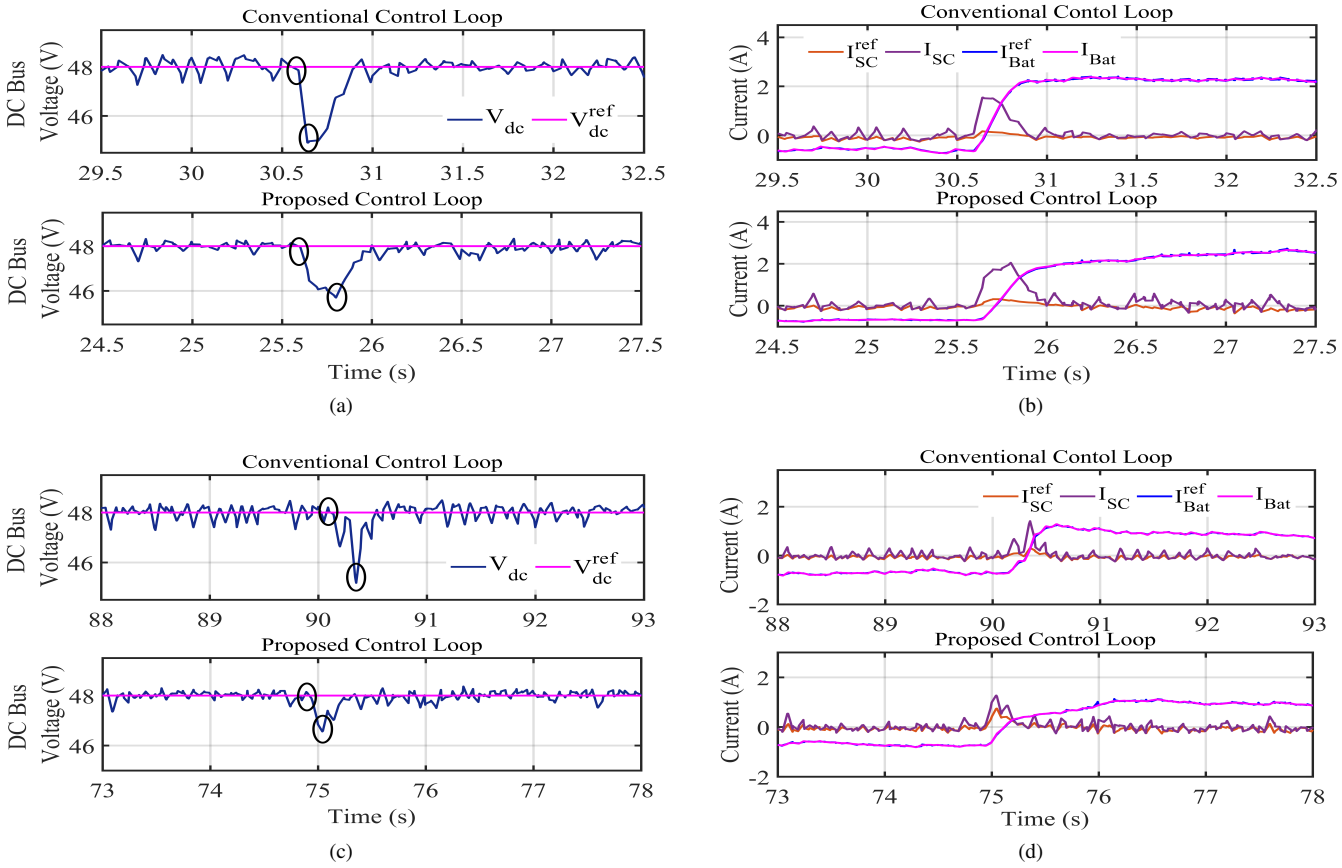

Fig. 10: Comparative results of conventional and proposed controller under sudden load change (a) DC bus voltage (b) battery and SC current. Comparative analysis of proposed and conventional controller under sudden wind speed change (c) DC bus voltage, (d) battery and SC current

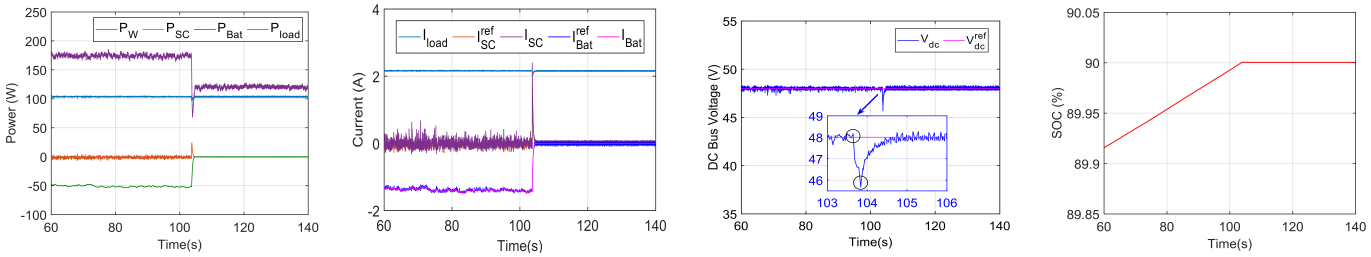

Fig. 11: Proposed controller results for battery shut-down mode for $SOC \geq 90\%$ (a) power, (b) battery current, (c) DC bus voltage, (d) %SOC.

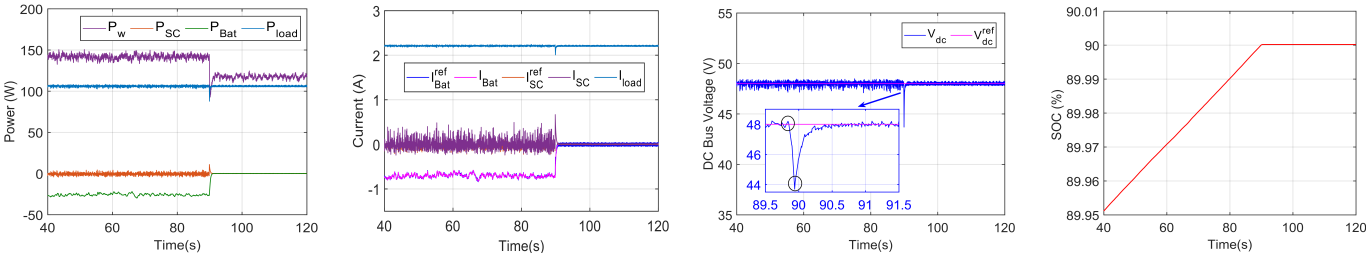

Fig. 12: Conventional controller results for battery shut-down mode for $SOC \geq 90\%$ (a) power, (b) battery current, (c) DC bus voltage, (d) %SOC.

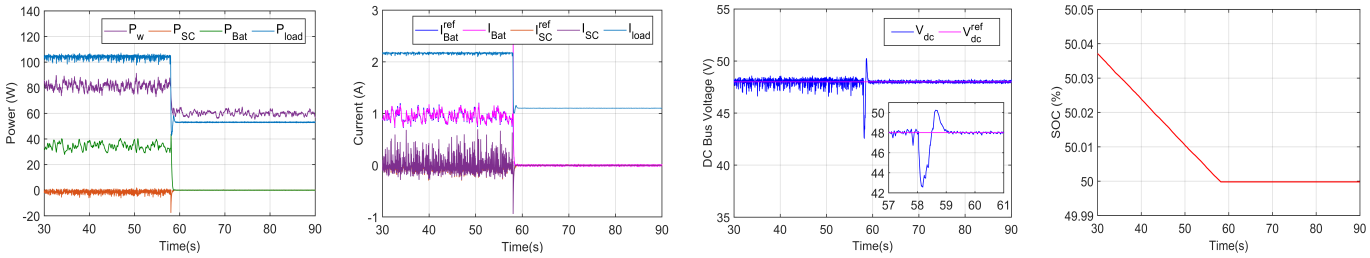

(a) (b) (c) (d)

Fig. 13: Proposed controller results for battery shut-down mode for $SOC \leq 50\%$ (a) power, (b) battery current, (c) DC bus voltage, (d) %SOC.

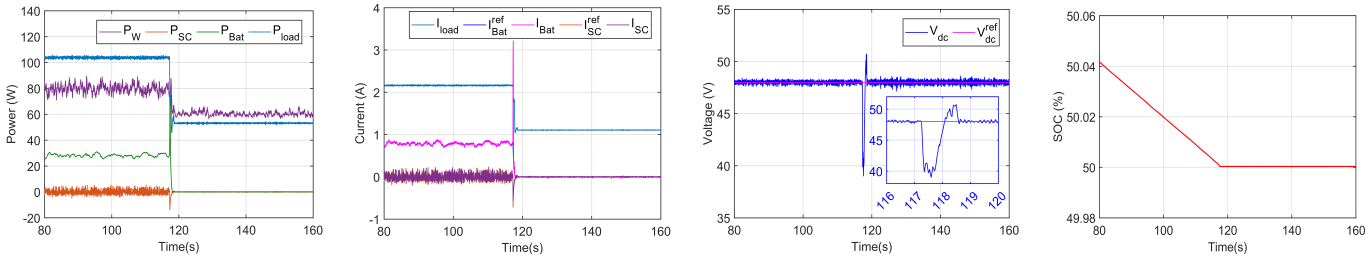

(a) (b) (c) (d)

Fig. 14: Conventional controller results for battery shut-down mode for $SOC \leq 50\%$ (a) power, (b) battery current, (c) DC bus voltage, (d) %SOC.

capable of maintaining the DC bus voltage at 48 V. A comparative analysis of conventional and proposed controller in terms of percentage overshoot (M_p), settling time (T_{set}) and steady-state error is depicted in Table IV. The analysis justifies better dynamic performance of the proposed PDCS with respect to the conventional one.

TABLE III: All possible modes of the proposed PDCS with their corresponding power balance and reference current setting

Sl.No	Operating Mode	Time (s)	Working Mode	Power Balance Eq.	Reference Current
1.	Normal Operating Mode (DF-MPPT) ($50 < SOC_{bat} < 90$) **(Fig. 8)**	(a) t = 0 s to 25.4 s (Wind speed = 6.5 m/s)	EGM	$P_{load}(t) = P_w(t) - P_{net}(t) - P_{loss}(t)$ where, $P_{load} = 104$ W, $P_w = 148$ W, $P_{net} = 30$ W, $P_{loss} = 14$ W	i_{bat_ref} = i_{avg} = -ve $i_{sc\_ref} = i_{hfc} + i_{osc}$
		(b) t = 25.4 s to 50.6 s (Wind speed = 6.5 m/s, Load increase)	DGM	$P_{load}(t) = P_w(t) + P_{net}(t) - P_{loss}(t)$ where, $P_{load} = 218$ W, $P_w = 148$ W, $P_{net} = 85$ W, $P_{loss} = 15$ W	i_{bat_ref} = i_{avg} = +ve $i_{sc\_ref} = i_{hfc} + i_{osc}$
		(c) t = 50.6 s to 75.03 s (Wind speed = 6.5 m/s, Load decrease)	EGM	$P_{load}(t) = P_w(t) - P_{net}(t) - P_{loss}(t)$ where, $P_{load} = 104$ W, $P_w = 148$ W, $P_{net} = 30$ W, $P_{loss} = 14$ W	i_{bat_ref} = i_{avg} = -ve $i_{sc\_ref} = i_{hfc} + i_{osc}$
		(d) t = 75.03 s to 99.83 s (Wind speed = 5.5 m/s)	DGM	$P_{load}(t) = P_w(t) + P_{net}(t) - P_{loss}(t)$ where, $P_{load} = 104$ W, $P_w = 84$ W, $P_{net} = 34$ W, $P_{loss} = 14$ W	i_{bat_ref} = i_{avg} = +ve $i_{sc\_ref} = i_{hfc} + i_{osc}$
		(e) t = 99.83 s to 126 s (Wind speed = 6 m/s)	FPM	$P_{load}(t) = P_w(t) - P_{net}(t) - P_{loss}(t)$ where, $P_{load} = 104$ W, $P_w = 118$ W, $P_{net} = 0$ W, $P_{loss} = 14$ W	i_{bat_ref} = i_{avg} = 0 $i_{sc\_ref} = i_{hfc}$
		(f) t = 126 s to 150 s (Wind speed = 7 m/s)	EGM	$P_{load}(t) = P_w(t) - P_{net}(t) - P_{loss}(t)$ where, $P_{load} = 104$ W, $P_w = 180$ W, $P_{net} = 60$ W, $P_{loss} = 16$ W	i_{bat_ref} = i_{avg} = -ve $i_{sc\_ref} = i_{hfc} + i_{osc}$
2.	Battery Protection Mode ($SOC_{bat} \geq 90$) **(Fig. 11)**	(a) t = 60 s to 103.64 s (Wind speed = 7 m/s)	EGM	$P_{load}(t) = P_w(t) - P_{net}(t) - P_{loss}(t)$ where, $P_{load} = 104$ W, $P_w = 176$ W, $P_{net} = 54$ W, $P_{loss} = 18$ W	i_{bat_ref} = i_{avg} = -ve $i_{sc\_ref} = i_{hfc} + i_{osc}$
		(b) t = 103.64 s to 140 s (Wind speed = 7 m/s)	RPM	$P_{load}(t) = P_w(t) + P_{net}(t) - P_{loss}(t)$ where, $P_{load} = 104$ W, $P_w = 120$ W, $P_{net} = 0$ W, $P_{loss} = 16$ W	i_{bat_ref} = i_{avg} = 0 $i_{sc\_ref} = i_{hfc}$
3.	Battery Protection Mode ($SOC_{bat} \leq 50$) **(Fig. 13)**	(a) t = 80 s to 117.78 s (Wind speed = 5.5 m/s)	DGM	$P_{load}(t) = P_w(t) + P_{net}(t) - P_{loss}(t)$ where, $P_{load} = 104$ W, $P_w = 84$ W, $P_{net} = 34$ W, $P_{loss} = 14$ W	i_{bat_ref} = i_{avg} = +ve $i_{sc\_ref} = i_{hfc} + i_{osc}$
		(b) t = 117.78 s to 160 s (Wind speed = 5.5 m/s)	RPM	$P_{load}(t) = P_w(t) + P_{net}(t) - P_{loss}(t)$ where, $P_{load} = 51$ W, $P_w = 65$ W, $P_{net} = 0$ W, $P_{loss} = 14$ W	i_{bat_ref} = i_{avg} = 0 $i_{sc\_ref} = i_{hfc}$

TABLE IV: Comparative evaluation of conventional and proposed controller

Parameters	Conventional Controller	Proposed Controller
M_p (Load change)	7.12 %	4.75 %
M_p (Wind speed change)	5.81 %	2.20 %
M_p (SOC $\geq 90\%$)	8.97 %	4.25 %
M_p (SOC $\leq 50\%$)	24.29 %	13.7 %
Settling Time (T_{set})	0.8 s	0.6 s
Steady-state Error	1.24 %	0.45 %

V. Conclusion

This paper illustrates implementation of a novel PDCS for efficient power utilization in the autonomous LVDC microgrid driven by WPGS along with HESS. The PDCS accomplishes the power computation, reference current generation along with operating mode selection effectively. The coordinated operation of WPGS, HESS and load are achieved for different operating modes. The WPGS operates at optimum power with reduced steady-state oscillations and better dynamic performance during wind speed and load variations. The DC bus voltage is tightly regulated at 48 V despite of being subjected to different operating constraints (i.e. wind speed change, load variation, $SOC \geq 90\%$ and $SOC \leq 50\%$). The overall functionality of the SEIG based autonomous LVDC microgrid with HESS is found satisfactory.

References

[1] https://www.iea.org/policies/6528-energy-strategy-2050, accessed: 2022-06-03.

[2] R. M. Elavarasan, G. Shafiullah, S. Padmanaban, N. M. Kumar, A. Annam, A. M. Vetrichelvan, L. Mihet-Popa, and J. B. Holm-Nielsen, "A comprehensive review on renewable energy development, challenges, and policies of leading indian states with an international perspective," *IEEE Access*, vol. 8, pp. 74 432–74 457, 2020.

[3] F. Nejabatkhah and Y. W. Li, "Overview of power management strategies of hybrid ac/dc microgrid," *IEEE Transactions on Power Electronics*, vol. 30, no. 12, pp. 7072–7089, 2015.

[4] T. Dragičević, X. Lu, J. C. Vasquez, and J. M. Guerrero, "Dc microgrids—part ii: A review of power architectures, applications, and standardization issues," *IEEE Transactions on Power Electronics*, vol. 31, no. 5, pp. 3528–3549, 2016.

[5] M. S. Alam, F. S. Al-Ismail, A. Salem, and M. A. Abido, "High-level penetration of renewable energy sources into grid utility: Challenges and solutions," *IEEE Access*, vol. 8, pp. 190 277–190 299, 2020.

[6] J. Mishra, P. K. Behera, M. Pattnaik, and S. Samanta, "An efficient supervisory power management scheme for a windx2013;battery-assisted hybrid autonomous system," *IEEE Systems Journal*, pp. 1–12, 2022.

[7] X. Li, D. Hui, and X. Lai, "Battery energy storage station (bess)-based smoothing control of photovoltaic (pv) and wind power generation fluctuations," *IEEE transactions on sustainable energy*, vol. 4, no. 2, pp. 464–473, 2013.

[8] Y. Wang, L. Wang, M. Li, and Z. Chen, "A review of key issues for control and management in battery and ultra-capacitor hybrid energy storage systems," *ETransportation*, vol. 4, p. 100064, 2020.

[9] T. Ayodele, A. Ogunjuyigbe, and B. Olateju, "Improving battery lifetime and reducing life cycle cost of a pv/battery system using supercapacitor for remote agricultural farm power application," *Journal of renewable and Sustainable energy*, vol. 10, no. 1, p. 013503, 2018.

[10] Z. Song, J. Li, X. Han, L. Xu, L. Lu, M. Ouyang, and H. Hofmann, "Multi-objective optimization of a semi-active battery/supercapacitor energy storage system for electric vehicles," *Applied Energy*, vol. 135, pp. 212–224, 2014.

[11] J. Wang, P. Liu, J. Hicks-Garner, E. Sherman, S. Soukiazian, M. Verbrugge, H. Tataria, J. Musser, and P. Finamore, "Cycle-life model for graphite-lifepo4 cells," *Journal of power sources*, vol. 196, no. 8, pp. 3942–3948, 2011.

[12] S. B. Peterson, J. Apt, and J. Whitacre, "Lithium-ion battery cell degradation resulting from realistic vehicle and vehicle-to-grid utilization," *Journal of Power Sources*, vol. 195, no. 8, pp. 2385–2392, 2010.

[13] W. Zuo, R. Li, C. Zhou, Y. Li, J. Xia, and J. Liu, "Battery-supercapacitor hybrid devices: recent progress and future prospects," *Advanced science*, vol. 4, no. 7, p. 1600539, 2017.

[14] W. Jing, C. H. Lai, W. S. Wong, and M. D. Wong, "A comprehensive study of battery-supercapacitor hybrid energy storage system for standalone pv power system in rural electrification," *Applied Energy*, vol. 224, pp. 340–356, 2018.

[15] A. Lahyani, P. Venet, A. Guermazi, and A. Troudi, "Battery/supercapacitors combination in uninterruptible power supply (ups)," *IEEE Transactions on Power Electronics*, vol. 28, no. 4, pp. 1509–1522, 2013.

[16] W. Jing, C. H. Lai, S. H. W. Wong, and M. L. D. Wong, "Battery-supercapacitor hybrid energy storage system in standalone dc microgrids: A review," *IET Renewable Power Generation*, vol. 11, no. 4, pp. 461–469, 2017.

[17] Q. Zhang and G. Li, "Experimental study on a semi-active battery-supercapacitor hybrid energy storage system for electric vehicle application," *IEEE Transactions on Power Electronics*, vol. 35, no. 1, pp. 1014–1021, 2020.

[18] L. Sun, K. Feng, C. Chapman, and N. Zhang, "An adaptive power-split strategy for battery–supercapacitor powertrain—design, simulation, and experiment," *IEEE Transactions on Power Electronics*, vol. 32, no. 12, pp. 9364–9375, 2017.

[19] T. S. Babu, K. R. Vasudevan, V. K. Ramachandaramurthy, S. B. Sani, S. Chemud, and R. M. Lajim, "A comprehensive review of hybrid energy storage systems: Converter topologies, control strategies and future prospects," *IEEE Access*, vol. 8, pp. 148 702–148 721, 2020.

[20] D. B. W. Abeywardana, B. Hredzak, V. G. Agelidis, and G. D. Demetriades, "Supercapacitor sizing method for energy-controlled filter-based hybrid energy storage systems," *IEEE Transactions on Power Electronics*, vol. 32, no. 2, pp. 1626–1637, 2017.

[21] Q. Zhang, L. Wang, G. Li, and Y. Liu, "A real-time energy management control strategy for battery and supercapacitor hybrid energy storage systems of pure electric vehicles," *Journal of Energy Storage*, vol. 31, p. 101721, 2020.

[22] Y. Zhang, G. Du, and Y. Lei, "Deadbeat control with power sharing for supercapacitor/ battery-based hybrid energy storage systems in dc microgrids," in *IECON 2020 The 46th Annual Conference of the IEEE Industrial Electronics Society*, 2020, pp. 1785–1790.

[23] P. Singh and J. Lather, "Dynamic current sharing, voltage and soc regulation for hess based dc microgrid using cpismc technique," *Journal of Energy Storage*, vol. 30, p. 101509, 2020.

[24] K. Bi, G. Zhang, R. Xie, and B. Peng, "Improved droop control based on supercapacitor voltage of hybrid energy storage system in bipolar dc microgrid," in *2020 5th Asia Conference on Power and Electrical Engineering (ACPEE)*, 2020, pp. 548–554.

[25] P. Nambisan and M. Khanra, "Optimal energy management of battery supercapacitor aided solar pv powered agricultural feed mill using pontryagin's minimum principle," *IEEE Transactions on Power Electronics*, vol. 37, no. 2, pp. 2216–2225, 2021.

[26] N. R. Tummuru, M. K. Mishra, and S. Srinivas, "Dynamic energy management of hybrid energy storage system with high-gain pv converter," *IEEE Transactions on Energy Conversion*, vol. 30, no. 1, pp. 150–160, 2015.
[27] S. Sikkabut, P. Mungporn, C. Ekkaravarodome, N. Bizon, P. Tricoli, B. Nahid-Mobarakeh, S. Pierfederici, B. Davat, and P. Thounthong, "Control of high-energy high-power densities storage devices by li-ion battery and supercapacitor for fuel cell/photovoltaic hybrid power plant for autonomous system applications," *IEEE Transactions on Industry Applications*, vol. 52, no. 5, pp. 4395–4407, 2016.
[28] B. R. Ravada and N. R. Tummuru, "Control of a supercapacitor-battery-pv based stand-alone dc-microgrid," *IEEE Transactions on Energy Conversion*, vol. 35, no. 3, pp. 1268–1277, 2020.
[29] Y. S. Perdana, S. M. Muyeen, A. Al-Durra, H. K. Morales-Paredes, and M. G. Simões, "Direct connection of supercapacitor–battery hybrid storage system to the grid-tied photovoltaic system," *IEEE Transactions on Sustainable Energy*, vol. 10, no. 3, pp. 1370–1379, 2019.
[30] G. Wang, M. Ciobotaru, and V. G. Agelidis, "Power smoothing of large solar pv plant using hybrid energy storage," *IEEE Transactions on Sustainable Energy*, vol. 5, no. 3, pp. 834–842, 2014.
[31] S. Augustine, M. K. Mishra, and N. Lakshminarasamma, "A unified control scheme for a standalone solar-pv low voltage dc microgrid system with hess," *IEEE Journal of Emerging and Selected Topics in Power Electronics*, vol. 8, no. 2, pp. 1351–1360, 2020.
[32] R. W. Erickson and D. Maksimovic, *Fundamentals of power electronics*. Springer Science & Business Media, 2007.
[33] P. T. Krein, "Elements of power electronics," 1998.
[34] M. C. Joshi and S. Samanta, "Energy management with improved frequency sharing based control for battery/ultracapacitor hybrid energy system in the presence of delay," *IET Power Electronics*, vol. 13, no. 10, pp. 2019–2028, 2020.
[35] J. Mishra, M. Pattnaik, and S. Samanta, "Drift-free perturb and observe mppt algorithm with improved performance for seig-based stand-alone wind energy generation system," *IEEE Transactions on Power Electronics*, vol. 35, no. 6, pp. 5842–5849, 2020.
[36] P. K. S. Roy, H. B. Karayaka, Y. Yan, and Y. Alqudah, "Investigations into best cost battery-supercapacitor hybrid energy storage system for a utility scale pv array," *Journal of Energy Storage*, vol. 22, pp. 50–59, 2019.